

# Electromagnetic Compatibility Study of Quadcopter UAVs: Characteristic Mode Analysis of the Frame's Material and Shape Effect

Mohamed Z. M. Hamdalla<sup>1, 2, \*</sup>, Jesus M. Roacho-Valles<sup>1</sup>,  
Anthony N. Caruso<sup>2</sup>, and Ahmed M. Hassan<sup>1, 2</sup>

**Abstract**—The variation in flight attitude, line-of-sight, and speed of unmanned aerial vehicles (UAVs) affect their polarization-dependent coupling cross-section and resultant compatibility to pulsed electromagnetic energy. Here, we present the out-of-band electromagnetic compatibility (EMC) effects of UAV frame material and shape on the UAV subcomponents. Characteristic mode analysis (CMA) is employed to study the fundamental modes supported by UAVs which facilitate the interpretation of its electromagnetic response and the prediction of its effect on the nearby components. Using CMA, we develop a framework that optimizes the placement of wires and traces of printed circuit boards (PCBs) on the frame mitigating interference from undesired electromagnetic sources. A 3-D scanner is used to provide four versions of a quadrotor UAV to study the frame shape effect on the coupling. Materials of differing permittivity are assigned to these frame versions to assist in understanding the material effect on the EM coupling to the UAV.

## 1. INTRODUCTION

Unmanned aerial vehicles (UAVs) perform a wide range of civilian and military-related applications [1–4]. UAVs fly in a highly congested wireless spectrum environment due to their recent use as mobile base stations [5–7]. Therefore, UAVs are prone to Electromagnetic Interference (EMI) from unintentional sources [8], which can lead to catastrophic consequences [9]. Therefore, quantifying the coupling to UAVs in the presence of unintentional radiations is essential.

EMI coupling pathways to any Device Under Test (DUT) can be classified into two categories: front-door coupling and back-door coupling [10]. Front-door coupling is the interference through the DUT's intended receiving elements, such as antennas and sensors. In contrast, the back-door coupling is interference through cables, traces, and slots not intended for electromagnetic reception, which is more challenging to predict and mitigate. The coupling to the UAV components through its receiving antennas is studied extensively in [11]. Moreover, Li et al. investigated different techniques to minimize such coupling and interference [12]. Besides, in [13], low-level direct drive (LLDD) and low-level swept fields (LLSF) methods have been applied to test a UAV with cables to assist in the measurements of EM interference. Interestingly, the analysis in [13] illustrated that the UAV cavity resonances play a significant role in the coupling to the enclosed cables. Therefore, the effect of the UAV frame on the electromagnetic interference to the UAV subcomponents needs to be considered. On the other hand, quantifying the electromagnetic response of the UAV is complicated by their permutations of shapes, sizes, and material compositions. In this work, we applied CMA to calculate the fundamental modes of perfectly conducting and dielectric UAV frames.

---

*Received 29 June 2022, Accepted 18 July 2022, Scheduled 28 July 2022*

\* Corresponding author: Mohamed Z. M. Hamdalla (mhamdalla@mail.umkc.edu).

<sup>1</sup> Department of Computer Science and Electrical Engineering, University of Missouri-Kansas City Kansas City, MO 64110, USA.

<sup>2</sup> Missouri Institute for Defense & Energy, University of Missouri-Kansas City Kansas City, MO 64110, USA.

CMA has been extensively employed in designing antennas and analyzing the electromagnetic scattering characteristics of various structures [14–27]. Moreover, we recently employed CMA to study coupling and interference to wires and other 2-D structures [28–30]. However, applying CMA for complex shapes composed of one or more dielectric materials is still under development [31–37].

This paper applies CMA to quantify the EM response of a quadcopter UAV frame with different dielectric properties. The frame EM response guides the prediction of locations exhibiting maximum or minimum interference for any given incident wave. We then use this information to optimize the placement of the sensors and the placement of the wire and electronic systems on the UAV’s frame.

Preliminary version of this work was presented in [38]. In the following section, a brief discussion of CMA is introduced.

## 2. CHARACTERISTIC MODE ANALYSIS

CMA is a full-wave electromagnetic technique that decomposes the total surface current coupled to a scatterer into a set of fundamental modes called eigen-currents. It calculates the relative importance of each mode at any frequency [35]. The modes can be calculated using the following eigenvalue equation [39]:

$$\mathbf{X}(\mathbf{J}_n) = \lambda_n \mathbf{R}(\mathbf{J}_n) \quad (1)$$

where  $\mathbf{X}$  and  $\mathbf{R}$  are the imaginary and real parts of the MOM impedance matrix of the UAV model, respectively;  $\mathbf{J}_n$  is the eigen-current, and  $\lambda_n$  is the eigenvalue of mode  $n$ . All eigenvalues,  $\lambda_n$ , in Equation (1) are real [40]. The magnitude of the eigenvalue is inversely proportional to the radiation efficiency of the associated mode. Hence, the reactive power of the mode is proportional to the magnitude of the eigenvalue. Therefore, the mode resonates when  $\lambda_n = 0$ . In addition, the sign of the eigenvalue determines whether the mode contributes to storing magnetic energy ( $\lambda_n > 0$ ) or electric energy ( $\lambda_n < 0$ ) [40]. Equation (1) above is solved at every frequency to generate the corresponding  $\mathbf{J}_n$  and  $\lambda_n$  values. At any frequency, the total current coupled to a scatterer due to an incident field can be expressed as [41]:

$$\mathbf{I} = \sum_n \frac{V_n \mathbf{J}_n}{(1 + j\lambda_n)} \quad (2)$$

where  $V_n$  is the modal excitation coefficient. It represents the coupling between the incident fields and mode  $n$ . The modal excitation coefficient  $V_n$  can be calculated using the following integral over the outer surface of the scatterer [41]:

$$V_n = \iint \mathbf{J}_n \cdot \mathbf{E}^i ds \quad (3)$$

where  $\mathbf{E}^i$  is the incident electric field.

In this paper, the following parameters will be studied to facilitate the predictions of the optimum locations for the electronic systems above a quadcopter UAV:

1. Modal significance ( $MS_n$ ): is independent of the excitation, and it identifies the relative weight of mode  $n$ , i.e., it describes the significance of its contribution to the UAV’s total coupled current. It can be calculated as:

$$MS_n = \frac{1}{|1 + j\lambda_n|} \quad (4)$$

The  $MS_n$  has a maximum value of 1, which occurs when the eigenvalue  $\lambda_n$  has a value of zero, and the mode is resonating. At any frequency of interest, the ratio of the values of  $MS_n$  among different modes allows one to identify the modes that dominate the coupled current.

2. Eigen-currents or modal currents  $\mathbf{J}_n$ : identify the current distribution of each mode  $n$ . The modal currents illustrate each mode’s maximum and minimum current locations. The eigen-currents  $\mathbf{J}_n$  are also independent of the excitation.

It is important to reemphasize that the CMA parameters  $MS_n$  and  $\mathbf{J}_n$  are independent of the incident field. The dependency on the excitation is entirely encapsulated in the modal excitation coefficient  $V_n$ . As a result, CMA will give insight into the supported modes of the UAV frame and how to excite each

mode without the need to test all possible angles of incidence. Therefore, in contrast to the statistical approaches that require a long computational time [42, 43], CMA is a qualitative technique to assist the electromagnetic coupling and interference to complex geometries. The following sections apply CMA to a quadcopter frame to quantify the UAV shape and material effect on the coupling.

### 3. PARAMETERS THAT AFFECT THE COUPLING TO THE UAV SYSTEM

#### 3.1. UAV Shape Effect

UAVs are typically composed of many components, each contributing to the overall electromagnetic response. Modeling the entire UAV components will lead to a convoluted electromagnetic response. Therefore, it will be hard to isolate the contribution of each component to the overall electromagnetic response. Therefore, we divided the UAV into components and studied each component individually. Since the frame is typically the largest component of the UAV, it will dominate the response at low frequencies. Therefore we focus our work in this paper on studying the electromagnetic response of UAV frames. Perfect Electric Conducting (PEC) material is assigned to the frame since most metals can be modeled as PEC at low frequency. In this section, we focused our analysis on the simple quadcopter UAV shown in Figure 1.

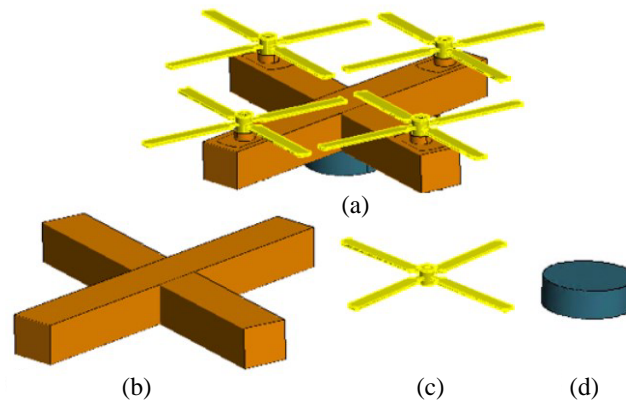


**Figure 1.** (a) Full UAV design, (b) UAV frame, (c) UAV blades, and (d) UAV transmitting and receiving system.

Two identical bars in a cross formation were constructed to construct the UAV frame in Figure 1(b), and the CMA was performed for this structure. CMA was performed using the commercial full-wave solver FEKO [45]. The single bar dimensions are 0.2 m, 0.028 m, and 0.024 m. Figure 2(b) shows the modal significance of the first six modes of the cross-shaped UAV frame.

The modal significance in Figure 2(a) provides the relative importance of each mode. For example, at 0.6 GHz, Mode 1 and Mode 2 have a significance of 1, whereas all the other modes have a significance below 0.5. Thus, up to 0.68 GHz, the response is dominated by Mode 1 and/or Mode 2. Besides, the total current generated on the bars will be similar to Mode 1 and/or Mode 2. The dominant mode at this frequency range depends on the excitation of the modes. Beyond 0.68 GHz, other modes become significant, and the response will be due to a mixture of modes.

Figure 2(a) illustrates that Mode 1 and Mode 2 have an overlapping modal significance, indicating that they have equal significance at every frequency. This overlap arises from the symmetry of the structure and the identical dimensions of the two intersecting bars. To simplify the distinction between Mode 1 and Mode 2, we keep one bar and slightly modify the other bar to break the symmetry. We have added 1% of a single bar length to the modified bar. Hence, the dimensions of one bar are 0.2 m  $\times$  0.028 m  $\times$  0.024 m, while the other is 0.202 m  $\times$  0.028 m  $\times$  0.024 m. Figure 2(b) shows the modal significance of the first three modes of the cross-shaped nonsymmetric UAV frame. The frequency range in Figure 2(b) is up to 1 GHz to illustrate the slight frequency shift between Mode 1 and Mode 2 due to the slight change in the arm's dimensions. Clearly, Mode 1 and Mode 2 do not overlap.

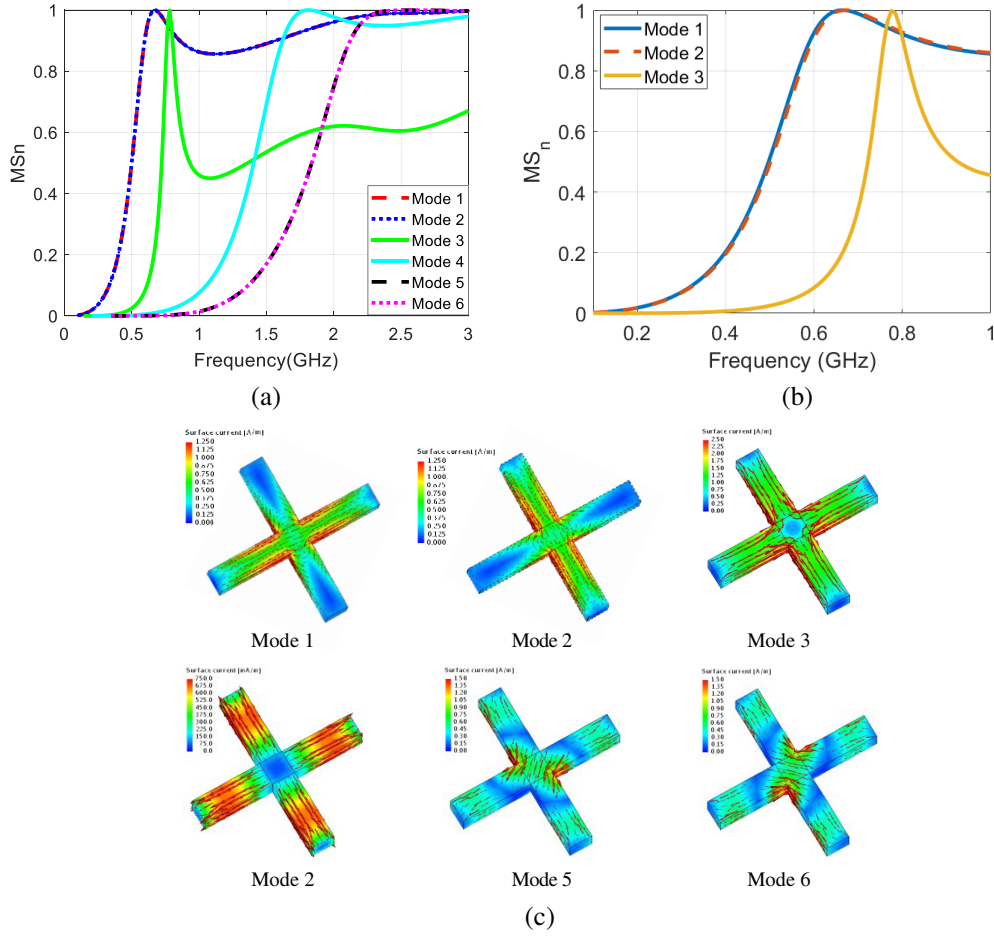


**Figure 2.** (a) Modal significance of the symmetric PEC cross-shaped UAV frame. (b) Modal significance of the first three modes of nonsymmetric PEC cross-shaped UAV frame. (c) Modal currents of the unequal arm length's PEC cross-shaped UAV frame.

Figure 2(c) shows the modal currents of the first six modes of the nonsymmetric UAV bars. The hot spots, shown in red in Figure 2(c), indicate the areas with the maximum currents. The UAV electronic devices near these spots will be more prone to coupling. The blue regions in Figure 2(c) show currents with low magnitudes. For the nonsymmetric UAV frame, Mode 1 will exhibit significant currents only in the horizontal bar, whereas in Mode 2, only the vertical bar will exhibit significant currents. Therefore, Mode 1 will be excited if the incident field is parallel to the horizontal bar, and Mode 2 will be excited if the incident field is parallel to the vertical bar. In addition, a circularly polarized wave can excite both modes.

Modes 3 is a hybrid combination of Modes 1 and 2, and it resonates at higher frequencies, as shown in the modal significance in Figure 2(a). Modes 5 and 6 overlap as their current pattern is similar but rotated by 90. Because of the overlap in modal current at the joint part of the bars, it is expected that Modes 5 and 6 will have a hybrid Mode at a higher frequency. This behavior was previously reported in similar structures with 4-fold symmetry [45, 46].

To study more realistic UAV frames, we used the MakerBot Digitizer scanner to scan an F450 drone frame. The MakerBot scanner is a desktop 3D scanner with a small turntable where the object to be scanned is placed. It uses laser scanning technology to scan the object. Using the MakerBot Digitizer scanner, we developed four different 3D versions, V1–V4, of the UAV, with V1 being the coarsest. In contrast, Version 4 is the finest, as shown in Figure 3. That is, Version 4 is the most accurate scanned structure, and it includes most of the features of the actual UAV frame. The single-arm length of the scanned frames is 19.5 cm, and the overall frame size is  $51.1 \times 51.1$  cm.

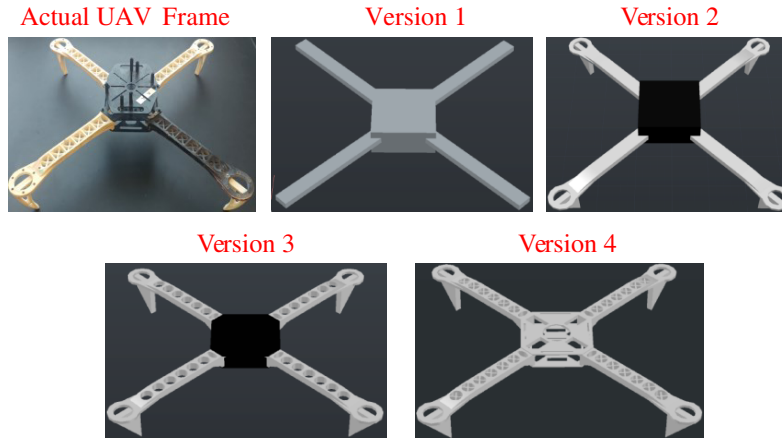


**Figure 3.** The actual frame of the UAV and four different 3D representations of its geometry.

CMA is applied to Version 1 of the frame to identify the resonance frequencies and the corresponding modal currents hot spots of the frame. Figure 4(a) shows the modal significance of the frame. Up to 0.5 GHz, the frame has three modes, two identical modes resonate at 0.29 GHz, and Mode 3 resonates at 0.32 GHz. The identical modes are due to the 4-fold symmetry of the UAV cross bars shape studied in the previous section. Figure 4(b) shows the normalized current distribution of the first three modes. The color bar in Figure 4(b) clarifies that the hotspots are near the arms; see the red colors. Moreover, the central square part of the UAV has no currents; see the blue color.

It is expected that the excited modes reradiate fields to the nearest subcomponents. Therefore, their relative location above the UAV frame will affect the coupling to the electronic devices. To demonstrate the effectiveness of CMA in quantifying such an effect, we studied the coupling to three identical wire loops. In modern PCB design, the signal transmission from one chip to another can form a loop due to the signal-return path loop. Therefore, the noise source in the circuit due to the external coupling can be modeled as a loop [47–49].

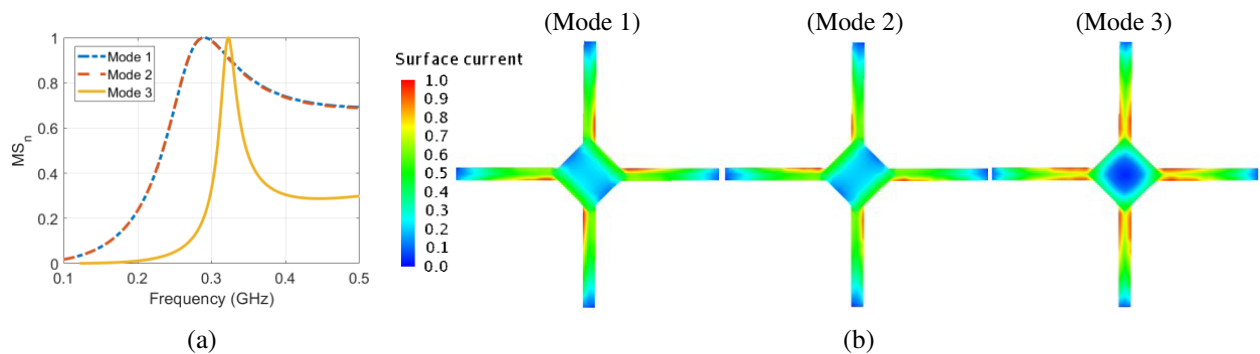


**Figure 4.** (a) Modal significance of the PEC frame (V1). (b) The normalized current distribution of the first three modes.

The loops have length 100 mm, radius 0.25 mm, and height 15 mm. The three loops are mounted at different locations above Version 1 of the UAV, as shown in Figure 5(a). The incident electric field is oriented parallel to the three loops, as shown in Figure 5(a). Figure 5(b) illustrates the loop configuration where two loads, Load 1 and Load 3, are connected at the terminals of the loop, and Load 2, is connected to the middle of the loop. All the loads are set to 50 Ω. Loads 1 and 3 represent the source’s internal and load resistance, respectively. Load 2 is attached as a crude representation of a measuring device to study the current/voltage on the transmission lines. A more accurate representation of the electronic devices on board will be investigated in future publications. Figure 5(c) shows the induced voltage at load 2. Loops 1 and 3 show higher overall induced voltage than loop 2 because they are above the

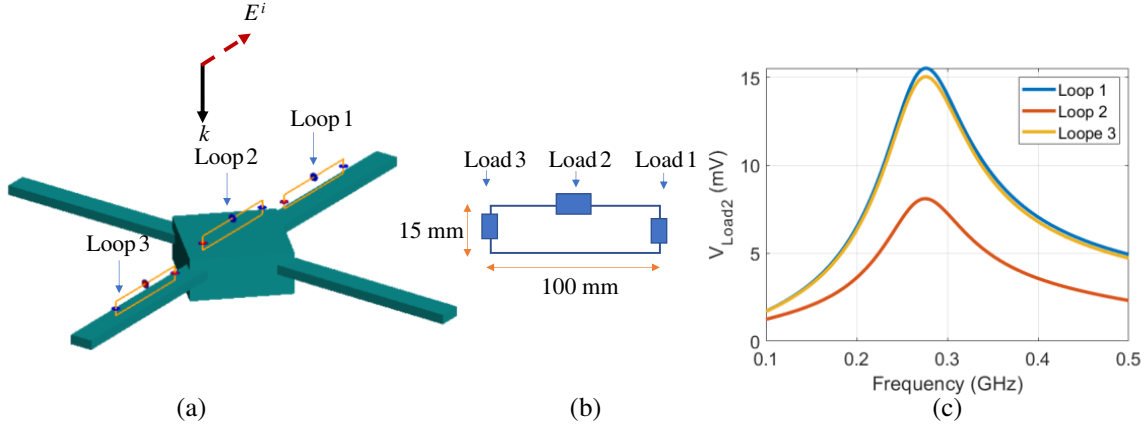


**Figure 5.** (a) Wire loops system above a PEC frame (V1) and the applied electric field orientation. (b) Sketch of the wire loop and its dimensions. (c) Induced voltage on load 2 of different wire loops above the PEC UAV frame.

“hotspots” of Mode 1, as shown in Figure 4(b). Thus, the predictions of the coupling sensitivity to the wire location above a complicated structure can be achieved using CMA. Therefore, we proceed to study the effect of different accurate representations of the UAV by applying CMA to the other three versions of the scanned UAV.

In this section, we study PEC frames, while more realistic dielectric properties will be studied in the next section. Figure 6(a) shows the effect of the small features captured by the high-resolution scanned UAV versions on the modal significance of the first mode, while its effect on mode 3 is shown in Figure 6(b). The small features captured by high-resolution versions are not significant on the resonance frequencies of the modes, as shown in Figure 6, except for V1 compared to the other versions. This is because V1 doesn't have the circular parts used to mount the motors at the end of each arm. Therefore, version 1 is electrically smaller than the other versions, which explains the difference in Figure 6. The study of Mode 2 is omitted since Mode 1 and Mode 2 are identical.

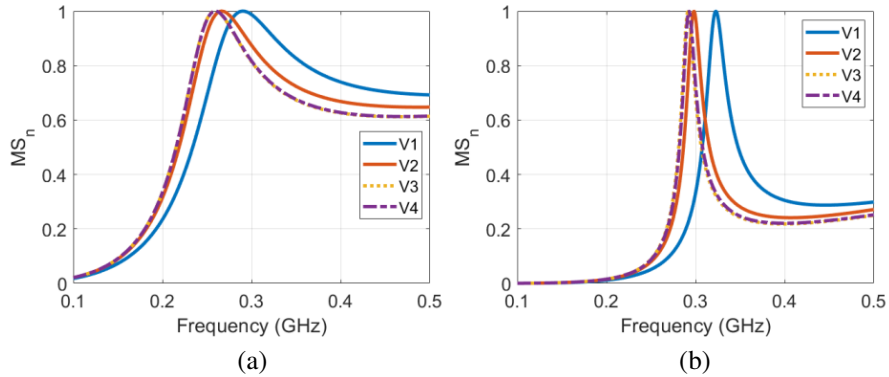


**Figure 6.** Modal significance of the four different 3D representations of the UAV frame. (a) Mode 1, (b) Mode 3.

On the other hand, each version has a different modal current distribution due to the geometrical difference. Figure 7 shows the current distribution of Mode 1 for the different scanned UAV versions. The blue regions in Figure 7 define low magnitude current, while the red regions represent the highest current magnitude. Figure 7 shows that the magnitude of the modal current increases as we move to a more accurate UAV representation. That is, V4 shows the highest magnitude of the modal current while V1 has the lowest magnitude. Thus, the geometrical differences between the versions affect the current distribution of Mode 1. As a result, they are affecting the coupling to wires and electronics at

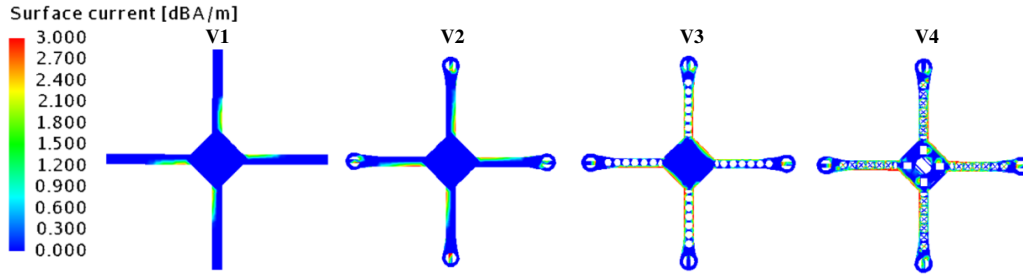


**Figure 7.** Current distribution of Mode 1 for different scanned versions of the UAV.

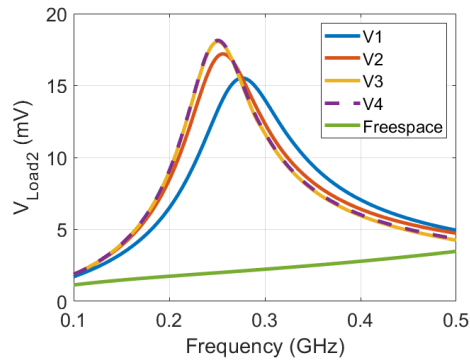


**Figure 8.** The induced voltage at load 2 on loop 1 above the four different 3D representations of the PEC UAV frame compared to the load voltage if the loops are in free space.

different locations above the frame. Three-wire loops are mounted at the same spots above the four UAV versions to demonstrate the effect of the geometrical differences. The excitation field direction and the loop locations are identical to the case in Figure 5(a). Since the magnitude of the modal current of V4 is the highest, it is expected that the induced voltages across the loops above V4 to be the highest. Oppositely, the modal current of V1 is the lowest. Therefore, the load voltages are expected to be the lowest in V1. Figure 8 shows the induced voltage across load 2 on the loop above the hotspot of Mode 1 for the four different UAV frame versions. Clearly, the induced voltage on the loop above the hotspot of Mode 1 of V4 is the highest, while the induced voltage on the loop located above the same spot on V1 is the lowest. Next, the induced voltage on the loops above the PEC frames is compared to that of the same loop configuration in free space. For the free space case, the frame is completely removed, and the induced voltages on loads of the loop are calculated. The comparison in Figure 8 illustrates that the induced voltage at the loops will only occur at the resonance frequency of the frame, and no peak will arise on the induced voltage of the loops in free space.

The analysis in this section illustrates the significance of small UAV frame features on the location optimization of the wires and electronics. It also illustrates the ability of CMA to optimize the location of the UAV subcomponents.

It is worth reemphasizing that the modal currents and modal significance are excitation-independent. Thus, all the predictions performed in this section do not need stochastic analysis for location optimization, which proves the computational efficiency of the CMA compared to traditional computational techniques. In the next section, materials of differing permittivity are assigned to the frame versions to assist in understanding the material effect on the EM coupling to the UAV.

### 3.2. UAV Material Effect

In this section, we perform CMA on the first two representations of the scanned UAV model in Figure 3, but we change their material properties to match the realistic dielectric properties of typical UAV frame

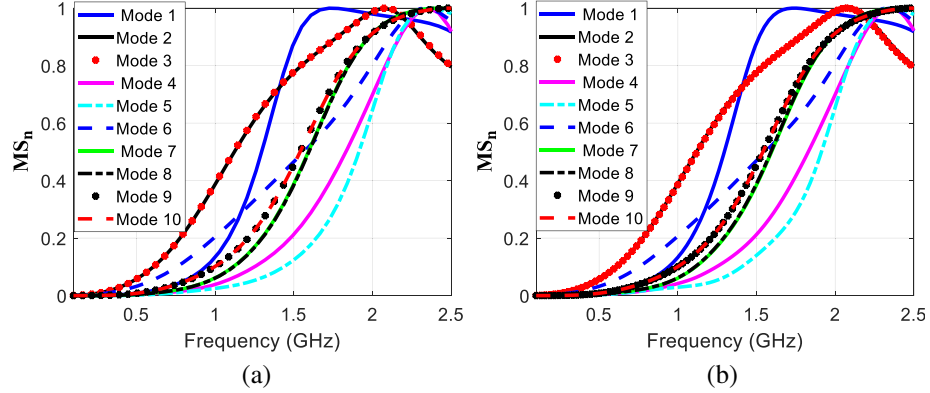


**Figure 9.** Modal significance of a dielectric UAV frame. (a) The 1st version. (b) The 2nd version.

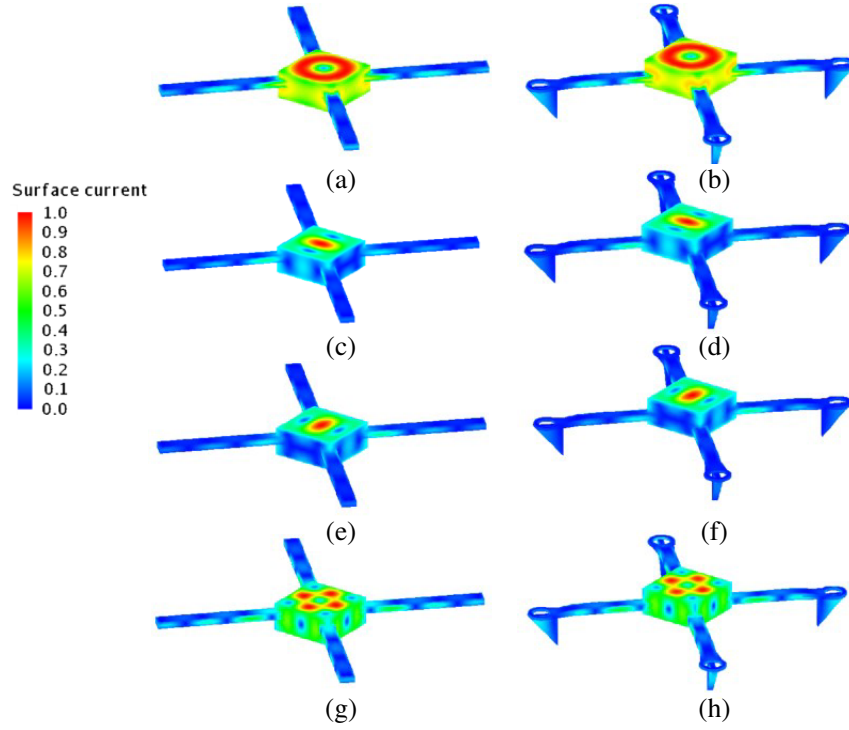


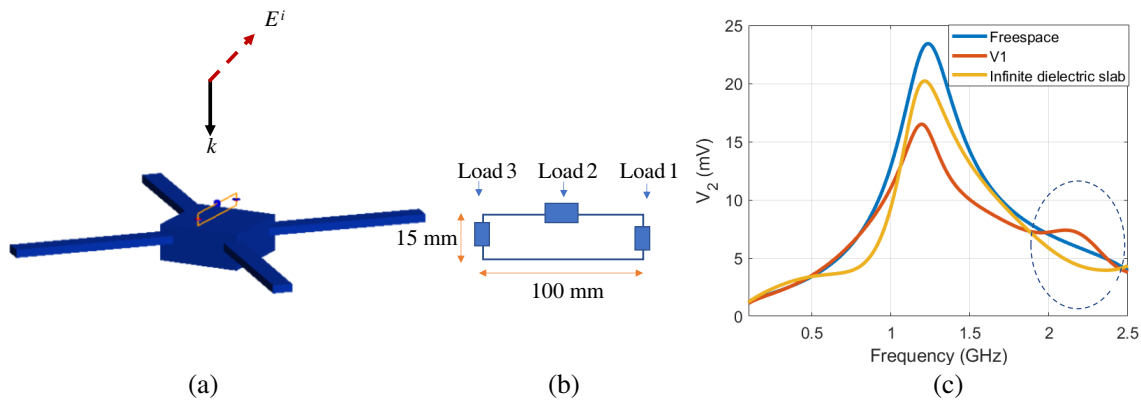
**Figure 10.** The normalized current distribution of (a) Mode 1, (c) Mode 2, (e) Mode 3, (g) Mode 4 for the 1st version of the dielectric UAV frame. (b) Mode 1, (d) Mode 2, (f) Mode 3, (h) Mode 4 for the 2nd version of the dielectric UAV frame.

plastics ( $\epsilon_r \approx 3.3$ ). The modal significance of the two versions is shown in Figure 9. Although version 2 has extra pieces at the arms of the UAV, the modal significance of both versions is identical. Figure 9 illustrates that the response of the dielectric UAV frame is less sensitive to the physical features of the arms.

The distributions of the modal currents for both versions of the UAV are shown in Figure 10. The current distributions of the modes are concentrated in the central part of the frame, contrary to the conducting frames. Therefore, changing the length/width of the arm has a minor contribution to the overall electrical path of the modal currents.

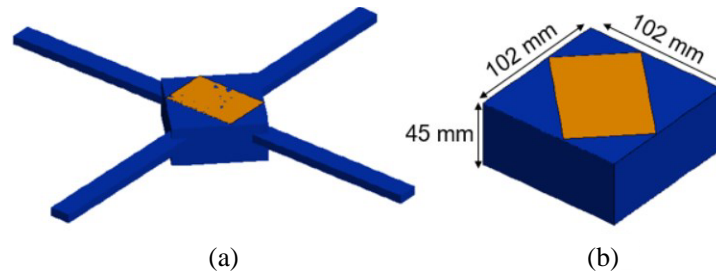
Similar to our previous discussions about the mode hybridization phenomena, the modal currents of Mode 2 and Mode 3 are identical. Still, Mode 3 is rotated by  $90^\circ$  around the axis of the UAV in comparison to Mode 2. Mode 4 is a hybrid combination of Mode 2 and Mode 3. Figure 9 and

Figure 10 illustrate that any electronic component on top of the central part of the UAV may be prone to coupling and interference. To demonstrate how the relative location of the electronic devices can affect their response, we studied coupling to wire loop in three cases. Firstly, the loop is mounted above V1 of the UAV with a 3 mm separation. Secondly, the loop is in free space, and thirdly the loop is placed 3 mm away from an infinite planar dielectric slab. The relative permittivity of the slab is  $\epsilon_r = 3.3$ , and its thickness is 45 mm, similar to the frame’s center part properties. The incident electric field is oriented to excite Mode 2 of the frame and parallel to the loop, as shown in Figure 11(a). Figure 11(b) shows a sketch of the wire loop and its dimensions. Figure 11(c) shows the induced voltage at load 2 in the three studied cases. The peak in the induced voltage of all the loops at 1.4 GHz corresponds to the resonance frequency of Mode 1 of the loop itself. Clearly, the relative permittivity of the frame/layer is responsible for the degradation in the coupling at 1.4 GHz. It is also responsible for the reduction in the bandwidth of the peak. The induced voltage on load 2 in free space and above the infinite dielectric slab has no peak around 2.2 GHz. However, load 2 of the loop above the UAV has the highest induced voltage corresponding to the modes of the frame, as illustrated in Figure 9.



**Figure 11.** (a) The loop above a dielectric frame (V1) and the applied electric field orientation. (b) Sketch of the wire loop and its dimensions. (c) Induced voltage on load 2 at the loop in free space, above of V1 of the UAV frame, and above an infinite planar dielectric slab.

Another advantage of the CMA is that it explicitly delineates the current distribution of the modes. This current distribution allows us to predict which modes are affected by a change in the UAV’s geometry. This study can facilitate simplifying yet maintaining an accurate representation of the frame. To illustrate how to employ CMA to save the computational time of simulating the frame with different electronic components, we simplified the frame to be computationally efficient for the EM analysis. The arms of the frame are removed, and only the body, where the modal currents are concentrated, is kept. CMA for both frame representations, shown in Figure 12, is performed. The two representations are assumed to have the same realistic dielectric properties as the typical UAV frame plastics ( $\epsilon_r = 3.3$ ). A crude representation of the bulk electronics above the UAV is modeled as a  $56 \times 85.6$  mm PEC sheet



**Figure 12.** (a) The 1st version. (b) Simplified representation of the dielectric UAV.

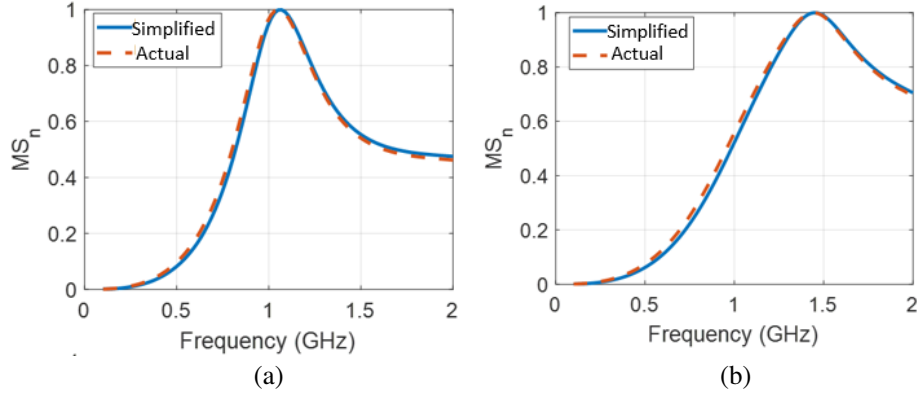


**Figure 13.** The modal significance of 1st version versus the simplified representation of the dielectric UAV. (a) Mode 1, (b) Mode 2.

above the two UAV representations. The modal significance of the two representations is shown in Figure 13. The modal significance of both representations is identical, while V1 has the arms of the UAV. The computational time of the CMA for the complete frame with arms is 38.9 hours, while it is 6.7 hours for the simplified frame. The analysis in this section shows that the knowledge of the modal behavior can simplify the problem's computational complexity. The following section clarifies the effect of varying the UAV frame dimensions on previously described modal behavior.

#### 4. SENSITIVITY OF MODES TO UAV MODEL DIMENSIONS AND MATERIAL

The dimensions of a UAV can vary in different models. Therefore, in this section, we explore how the modal characteristics vary with the dimensions and material of the UAV frame. Two dimensions of the UAV frame in Figure 14(a) are varied:  $\ell_a$  and  $\ell_b$ . The effect of varying the UAV's arm length  $\ell_a$  on the modal behavior for fixed center body dimension  $\ell_b = 100$  mm, is plotted in Figure 14(b). For this analysis, the arm length  $\ell_a$  is increased from 500 mm to 1000 mm in 100 mm increments. For each  $\ell_a$  value, we recalculated the modal significance,  $MS$ , of the first mode, and we plotted the resonance frequency of  $MS_1$  in Figure 14(b) (black line). The analysis in Figure 14(b) (black line) shows that the resonance frequency of Mode 1 is insensitive to the variation on the frame's arm since the current distribution of the first modes is concentrated at the body, not the arms, as explained in the previous section.

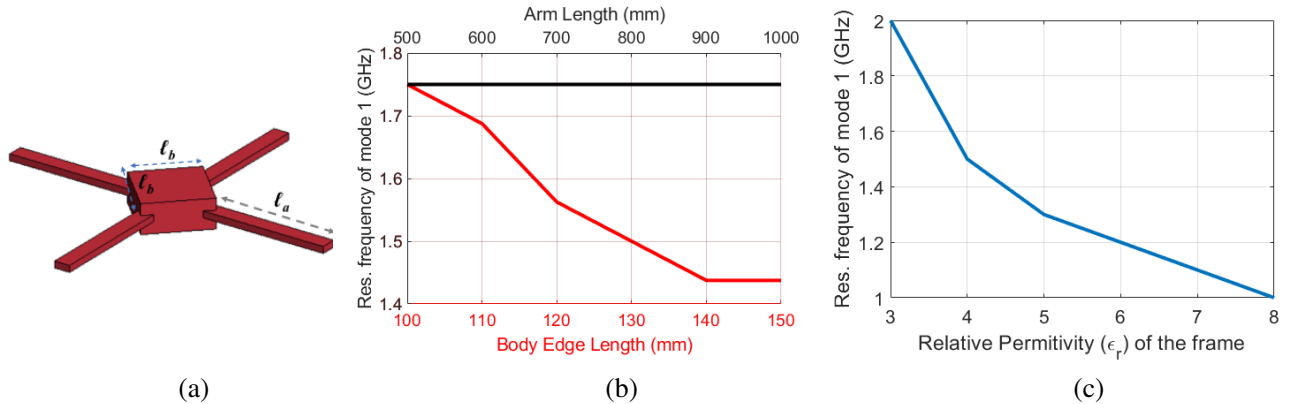


**Figure 14.** (a) A sketch of the quadcopter UAV showing the general dimensions of the structure. (b) The resonance frequencies of the modal significance of Mode 1 when the arm length and  $\ell_a$  body length  $\ell_b$  were varied. (c) When the dielectric properties of the frame were changed.

The effect of varying the length of the center body,  $\ell_b$ , for a fixed arm length,  $\ell_a = 500$  mm, is shown in Figure 14(b) (red line). As the body length  $\ell_b$  increases from 100 mm to 150 mm in 10 mm increments, the resonance frequency of Mode 1 decreases. The resonance frequency of Mode 1 is sensitive to the change in  $\ell_b$ , decreasing from 1.75 GHz to 1.44 GHz, corresponding to a 20% reduction in the resonance frequency for a 50% increase in the  $\ell_b$ .

The effect of the frame material on the resonance frequency of the modes is plotted in Figure 14(c). For this analysis, the arm length  $\ell_a = 500$ , the body length  $\ell_b = 100$  mm, and the relative permittivity of the frame varies from 3 to 8 in 1 increment. The resonance frequency of Mode 1 decreases from 2 GHz to 1 GHz, corresponding to a 50% reduction in the resonance frequency for a 166% increase in the relative permittivity of the frame  $\epsilon_r$ . The resonance frequency of the modes will decrease as the relative permittivity increases until it approaches the case of the PEC studied in the previous section.

## 5. CONCLUSION

In this work, we have studied the effects of quadcopter Unmanned Aerial Vehicles (UAVs) frame materials and shapes on the coupling and interference of the UAV subcomponents. A 3-D scanner is used to provide four versions of a quadrotor UAV to study the frame shape effect on the coupling. Characteristic Mode Analysis (CMA) was successfully applied to calculate the fundamental modes supported by the different versions of the UAV and the characteristics of these modes. The knowledge of this modal behavior facilitates optimizing the placement of wires and PCBs on the frame mitigating interference from undesired electromagnetic sources. The optimization process is based on a qualitative CMA, which is computationally efficient compared to statistical analysis. We showed that the coupling to the UAV subcomponents mounted at the center part of the dielectric UAV frame is the highest.

In contrast, the coupling to the UAV subcomponents mounted at the arms of the metallic UAV frame is the highest. Moreover, we optimized the computational time of the CMA of the UAV by efficiently reducing the complexity of the complete UAV frame. The optimization of the UAV complexity was guided by its modal behavior. In the future, we will extend the CMA approach employed herein to study more complicated and practical UAV models with a larger number of wires and electronics.

## ACKNOWLEDGMENT

This work is sponsored by ONR grants # N00014-17-1-2932 and # N00014-17-1-3016 and the University of Missouri-Kansas City, School of Graduate Studies Research Award.

## REFERENCES

1. Koo, V., Y. K. Chan, G. Vetharatnam, M. Y. Chua, C. H. Lim, C. S. Lim, C. C. Thum, T. S. Lim, Z. B. Ahmad, K. A. Mahmood, M. H. B. Shahid, C. Y. Ang, W. Q. Tan, P. N. Tan, K. S. Yee, W. G. Cheaw, H. S. Boey, A. L. Choo, and B. C. Sew, "A new unmanned aerial vehicle synthetic aperture radar for environmental monitoring," *Progress In Electromagnetics Research*, Vol. 122, 245–268, 2012.
2. Kawamoto, Y., H. Nishiyama, N. Kato, F. Ono, and R. Miura, "Toward future unmanned aerial vehicle networks: Architecture, resource allocation and field experiments," *IEEE Wireless Communications*, Vol. 26, No. 1, 94–99, Feb. 2019, doi: 10.1109/MWC.2018.1700368.
3. Intelligence, B. I., "Drones are about to fill the skies within the next 5 years," *Business Insider*, 2016.
4. Park, G., K. Park, and B. Song, "Spatio-temporal change monitoring of outside manure piles using unmanned aerial vehicle images," *Drones*, Vol. 5, No. 1, Art. No. 1, Mar. 2021, doi: 10.3390/drones5010001.
5. Li, B., Z. Fei, and Y. Zhang, "Uav communications for 5g and beyond: Recent advances and future trends," *IEEE Internet of Things Journal*, Vol. 6, No. 2, 2241–2263, Apr. 2019, doi: 10.1109/JIOT.2018.2887086.

6. González-Prelcic, N., R. W. Heath, C. Rusu, and A. Klautau, "High-capacity millimeter wave UAV communications," *UAV Communications for 5G and Beyond*, 203–229, John Wiley & Sons, Ltd., 2020, doi: 10.1002/9781119575795.ch8.
7. Abdel-Malek, M. A., N. Saputro, A. S. Ibrahim, and K. Akkaya, "Uav-assisted multi-path parallel routing for mmwave-based wireless networks," *Internet of Things*, Vol. 14, 100366, Jun. 2021, doi: 10.1016/j.iot.2021.100366.
8. Zhou, F., R. Wang, and J. Bian, "Joint trajectories and power allocation design for dual UAV-enabled secrecy SWIPT networks," *Progress In Electromagnetics Research M*, Vol. 87, 73–82, 2019.
9. "The role of drones in future terrorist attacks," *AUSA*, Feb. 26, 2021. <https://www.ausa.org/publications/role-drones-future-terrorist-attacks> (accessed Jun. 13, 2021).
10. Tortorich, R., "A comprehensive study on printed circuit board backdoor coupling in high intensity radiated fields environments," *LSU Doctoral Dissertations*, 5536, May 2021, doi: 10.31390/gradschool.dissertations.5536.
11. Zhang, D., M. Zhao, E. Cheng, and Y. Chen, "GPR-based emi prediction for UAV's dynamic datalink," *IEEE Transactions on Electromagnetic Compatibility*, Vol. 63, No. 1, 19–29, Feb. 2021, doi: 10.1109/TEM.2020.3000919.
12. Bo, L., Z. Shengbing, Y. Junpeng, and W. Liang, "An anti-interference method for about unmanned aerial vehicle flight data based on vxworks," *2016 IEEE Chinese Guidance, Navigation and Control Conference (CGNCC)*, 7–9, Aug. 2016, doi: 10.1109/CGNCC.2016.7828748.
13. Fernández Romero, S., P. López Rodríguez, D. Escot Bocanegra, D. Poyatos Martínez, and M. Añón Cancela, "Comparing open area test site and resonant chamber for unmanned aerial vehicle's high-intensity radiated field testing," *IEEE Transactions on Electromagnetic Compatibility*, Vol. 60, No. 6, 1704–1711, Dec. 2018, doi: 10.1109/TEM.2017.2747771.
14. Hassan, A. M., F. Vargas-Lara, J. F. Douglas, and E. J. Garboczi, "Electromagnetic resonances of individual single-walled carbon nanotubes with realistic shapes: A characteristic modes approach," *IEEE Transactions on Antennas and Propagation*, Vol. 64, No. 7, 2743–2757, Jul. 2016, doi: 10.1109/TAP.2016.2526046.
15. Durbhakula, K. C., et al., "Electromagnetic scattering from individual crumpled graphene flakes: A characteristic modes approach," *IEEE Transactions on Antennas and Propagation*, Vol. 65, No. 11, 6035–6047, Nov. 2017, doi: 10.1109/TAP.2017.2752218.
16. Dey, S., D. Chatterjee, E. J. Garboczi, and A. M. Hassan, "Plasmonic nanoantenna optimization using characteristic mode analysis," *IEEE Transactions on Antennas and Propagation*, Vol. 68, No. 1, 43–53, Jan. 2020, doi: 10.1109/TAP.2019.2938705.
17. Lau, B. K., M. Capek, and A. M. Hassan, "Characteristic modes: Progress, overview, and emerging topics," *IEEE Antennas and Propagation Magazine*, Vol. 64, No. 2, 14–22, Apr. 2022, doi: 10.1109/MAP.2022.3145719.
18. Manteuffel, D., F. H. Lin, T. Li, N. Peitzmeier, and Z. N. Chen, "Characteristic mode-inspired advanced multiple antennas: Intuitive insight into element-, interelement-, and array levels of compact large arrays and metantennas," *IEEE Antennas and Propagation Magazine*, Vol. 64, No. 2, 49–57, Apr. 2022, doi: 10.1109/MAP.2022.3145714.
19. Adams, J. J., S. Genovesi, B. Yang, and E. Antonino-Daviu, "Antenna element design using characteristic mode analysis: Insights and research directions," *IEEE Antennas and Propagation Magazine*, Vol. 64, No. 2, 32–40, Apr. 2022, doi: 10.1109/MAP.2022.3145718.
20. Chen, Y. and C. Wang, "Electrically small UAV antenna design using characteristic modes," *IEEE Transactions on Antennas and Propagation*, Vol. 62, No. 2, 535–545, Feb. 2014, doi: 10.1109/TAP.2013.2289999.
21. Sow, S., L. Guo, S. Zhou, and T. Chio, "Electrically small structural antenna design for small UAV based on characteristics modes," *2017 11th European Conference on Antennas and Propagation (EuCAP)*, 2134–2138, Mar. 2017, doi: 10.23919/EuCAP.2017.7928206.

22. Ma, R. and N. Behdad, "Design of platform-based hf direction-finding antennas using the characteristic mode theory," *IEEE Transactions on Antennas and Propagation*, Vol. 67, No. 3, 1417–1427, Mar. 2019, doi: 10.1109/TAP.2018.2884878.
23. Cao, Y. S., M. Ouyanz, Y. Wang, and J. Fan, "Emi modeling for antenna-chassis system using characteristic mode analysis," *2018 IEEE Symposium on Electromagnetic Compatibility, Signal Integrity and Power Integrity (EMC, SI PI)*, 181–186, Jul. 2018. doi: 10.1109/EMCSI.2018.8495389.
24. Yang, X., et al., "EMI radiation mitigation for heatsinks using characteristic mode analysis," *2018 IEEE Symposium on Electromagnetic Compatibility, Signal Integrity and Power Integrity (EMC, SI PI)*, 374–378, Jul. 2018, doi: 10.1109/EMCSI.2018.8495291.
25. Hamdalla, M. Z. M., et al., "Electromagnetic interference of unmanned aerial vehicles: A characteristic mode analysis approach," *2019 IEEE International Symposium on Antennas and Propagation and USNC-URSI Radio Science Meeting*, 553–554, Jul. 2019, doi: 10.1109/APUS-NCURSINRSM.2019.8888398.
26. Ückerseifer, J. and F. Gronwald, "Characteristic mode analysis of surface current distributions on metallic structures exposed to HIRF- and DCI-excitations," *Adv. Radio Sci.*, Vol. 18, 33–41, Dec. 2020, doi: 10.5194/ars-18-33-2020.
27. Rothenhäusler, M. and F. Gronwald, "Characteristic mode analysis of hirf- and dci-excitations of an aircraft structure," *2017 International Symposium on Electromagnetic Compatibility — EMC EUROPE*, 1–6, Sep. 2017, doi: 10.1109/EMCEurope.2017.8094764.
28. Hamdalla, M. Z. M., A. N. Caruso, and A. M. Hassan, "Predicting electromagnetic interference to a terminated wire using characteristic mode analysis," *2020 International Applied Computational Electromagnetics Society Symposium (ACES)*, 1–2, Jul. 2020, doi: 10.23919/ACES49320.2020.9196133.
29. Hamdalla, M., B. Bissen, A. N. Caruso, and M. Hassan, "Experimental validations of characteristic mode analysis predictions using GTEM measurements," *IEEE International Symposium on Antennas and Propagation and North American Radio Science Meeting*, 1799–1800, Montréal, Québec, Canada, Jul. 2020.
30. Hamdalla, M. Z. M., et al., "Characteristic mode analysis prediction and guidance of electromagnetic coupling measurements to a UAV model," *IEEE Access*, Vol. 10, 914–925, 2022, doi: 10.1109/ACCESS.2021.3138296.
31. Wu, Q., "Characteristic mode analysis of composite metallic-dielectric structures using impedance boundary condition," *IEEE Transactions on Antennas and Propagation*, Vol. 67, No. 12, 7415–7424, Dec. 2019, doi: 10.1109/TAP.2019.2934902.
32. Wu, Q., "Characteristic mode assisted design of dielectric resonator antennas with feedings," *IEEE Transactions on Antennas and Propagation*, Vol. 67, No. 8, 5294–5304, Aug. 2019, doi: 10.1109/TAP.2019.2916763.
33. Boyuan, M., S. Huang, J. Pan, Y.-T. Liu, D. Yang, and Y.-X. Guo, "Higher-order characteristic modes-based broad-beam dielectric resonator antenna," *IEEE Antennas and Wireless Propagation Letters*, Vol. 21, No. 4, 818–822, Apr. 2022, doi: 10.1109/LAWP.2022.3149603.
34. Huang, S., C.-F. Wang, J. Pan, and D. Yang, "Accurate sub-structure characteristic mode analysis of dielectric resonator antennas with finite ground plan," *IEEE Transactions on Antennas and Propagation*, Vol. 69, No. 10, 6930–6935, Oct. 2021, doi: 10.1109/TAP.2021.3070648.
35. Huang, S., J. Pan, C. Wang, Y. Luo, and D. Yang, "Unified implementation and cross-validation of the integral equation-based formulations for the characteristic modes of dielectric bodies," *IEEE Access*, Vol. 8, 5655–5666, 2020, doi: 10.1109/ACCESS.2019.2963278.
36. Guo, X.-Y., R.-Z. Lian, and M.-Y. Xia, "Variant characteristic mode equations using different power operators for material bodies," *IEEE Access*, Vol. 9, 62021–62028, 2021, doi: 10.1109/ACCESS.2021.3073901.
37. Huang, S., C.-F. Wang, J. Pan, D. Yang, and M.-C. Tang, "Full equiphase characteristic mode solution to lossless composite metallic-dielectric problems," *IEEE Transactions on Antennas and Propagation*, Vol. 69, No. 12, 8526–8538, Dec. 2021, doi: 10.1109/TAP.2021.3090791.

38. Hamdalla, M. Z. M., A. M. Hassan, and A. N. Caruso, "Characteristic mode analysis of the effect of the UAV frame material on coupling and interference," *2019 IEEE International Symposium on Antennas and Propagation and USNC-URSI Radio Science Meeting*, 1497–1498, Jul. 2019, doi: 10.1109/APUSNCURSINRSM.2019.8888344.
39. Harrington, R. and J. Mautz, "Theory of characteristic modes for conducting bodies," *IEEE Transactions on Antennas and Propagation*, Vol. 19, No. 5, 622–628, Sep. 1971, doi: 10.1109/TAP.1971.1139999.
40. Cabedo-Fabres, M., E. Antonino-Daviu, A. Valero-Nogueira, and M. F. Bataller, "The theory of characteristic modes revisited: A contribution to the design of antennas for modern applications," *IEEE Antennas and Propagation Magazine*, Vol. 49, No. 5, 52–68, Oct. 2007, doi: 10.1109/MAP.2007.4395295.
41. Chang, Y. and R. Harrington, "A surface formulation for characteristic modes of material bodies," *IEEE Transactions on Antennas and Propagation*, Vol. 25, No. 6, 789–795, Nov. 1977, doi: 10.1109/TAP.1977.1141685.
42. Gaynutdinov, R. R., I. V. Suzdaltsev, and S. F. Chermoshentsev, "Optimization unmanned aerial vehicle onboard equipment placement," *2020 International Russian Automation Conference (RusAutoCon)*, 1000–1004, Sep. 2020. doi: 10.1109/RusAutoCon49822.2020.9208172.
43. Makeev, P., "Two-level algorithm for automated placement of elements on a flex-rigid printed circuit board," *2021 International Conference on Electrotechnical Complexes and Systems (ICOECS)*, 196–201, Nov. 2021, doi: 10.1109/ICOECS52783.2021.9657330.
44. "Electromagnetic simulation software — altair feko," <https://altairhyperworks.com/product/FEKO>.
45. Garbacz, R. and E. Newman, "Characteristic modes of a symmetric wire cross," *IEEE Transactions on Antennas and Propagation*, Vol. 28, No. 5, 712–715, Sep. 1980, doi: 10.1109/TAP.1980.1142388.
46. Peitzmeier, N. and D. Manteuffel, "Upper bounds and design guidelines for realizing uncorrelated ports on multimode antennas based on symmetry analysis of characteristic modes," *IEEE Transactions on Antennas and Propagation*, Vol. 67, No. 6, 3902–3914, Jun. 2019, doi: 10.1109/TAP.2019.2905718.
47. Hubing, T., "PCB EMC design guidelines: A brief annotated list," *2003 IEEE Symposium on Electromagnetic Compatibility. Symposium Record (Cat. No.03CH37446)*, Vol. 1, 34–36, Aug. 2003, doi: 10.1109/ISEMC.2003.1236559.
48. Doridant, A., et al., "EMC of DSI3 communication protocol — PCB Consideration for Sensor product," *2017 International Symposium on Electromagnetic Compatibility — EMC EUROPE*, 1–6, Sep. 2017, doi: 10.1109/EMCEurope.2017.8094646.
49. Rehpade, R., S. D. Pable, and G. K. Kharate, "Design issues & challenges with EMI/EMC in system on packages (SOPs)," *2017 International conference of Electronics, Communication and Aerospace Technology (ICECA)*, Vol. 1, 335–338, Apr. 2017, doi: 10.1109/ICECA.2017.8203699.